Digital-resolution detection of microRNA with single-base selectivity by photonic resonator absorption microscopy

Taylor D. Canady[a,b,1], Nantao Li[b,c,1], Lucas D. Smith[b,d], Yi Lu[e], Manish Kohli[f,g], Andrew M. Smith[a,b,d,h,i], and Brian T. Cunningham[a,b,c,d,2]

[a]Institute for Genomic Biology, University of Illinois at Urbana–Champaign, Urbana, IL 61801; [b]Holonyak Micro and Nanotechnology Laboratory, University of Illinois at Urbana–Champaign, Urbana, IL 61801; [c]Department of Electrical and Computer Engineering, University of Illinois at Urbana–Champaign, Urbana, IL 61801; [d]Department of Bioengineering, University of Illinois at Urbana–Champaign, Urbana, IL 61801; [e]Department of Chemistry, University of Illinois at Urbana–Champaign, Urbana, IL 61801; [f]Department of Oncology, Mayo Clinic, Rochester, MN 55905; [g]Department of Genitourinary Oncology, H. Lee Moffitt Cancer Center, Tampa, FL 12902; [h]Department of Materials Science, University of Illinois at Urbana–Champaign, Urbana, IL 61801; and [i]Carle Illinois College of Medicine, University of Illinois at Urbana–Champaign, Urbana, IL 61801

Edited by John A. Rogers, Northwestern University, Evanston, IL, and approved August 15, 2019 (received for review March 20, 2019)

Circulating exosomal microRNA (miR) represents a new class of blood-based biomarkers for cancer liquid biopsy. The detection of miR at a very low concentration and with single-base discrimination without the need for sophisticated equipment, large volumes, or elaborate sample processing is a challenge. To address this, we present an approach that is highly specific for a target miR sequence and has the ability to provide "digital" resolution of individual target molecules with high signal-to-noise ratio. Gold nanoparticle tags are prepared with thermodynamically optimized nucleic acid toehold probes that, when binding to a target miR sequence, displace a probe-protecting oligonucleotide and reveal a capture sequence that is used to selectively pull down the target-probe–nanoparticle complex to a photonic crystal (PC) biosensor surface. By matching the surface plasmon-resonant wavelength of the nanoparticle tag to the resonant wavelength of the PC nanostructure, the reflected light intensity from the PC is dramatically and locally quenched by the presence of each individual nanoparticle, enabling a form of biosensor microscopy that we call Photonic Resonator Absorption Microscopy (PRAM). Dynamic PRAM imaging of nanoparticle tag capture enables direct 100-aM limit of detection and single-base mismatch selectivity in a 2-h kinetic discrimination assay. The PRAM assay demonstrates that ultrasensitivity (<1 pM) and high selectivity can be achieved on a direct readout diagnostic.

biosensors | photonics | nanotechnology | diagnostics | liquid biopsy

The development of rapid and cost-effective diagnostics is essential for disseminating technologies for clinical applications in broad point-of-care settings (1). The prominent rise of liquid-biopsy approaches to establish early disease detection, monitoring of treatments, prognostication, and predicting pretreatment outcomes further emphasizes the need for inexpensive high-performance assays (2). Among the numerous analytes in blood, circulating microRNA (miR) is an intriguing biomarker, with several studies correlating miR amount and variance to a cancer type and metastatic state (3–6). However, the standard protocol of whole-blood RNA isolation and purification followed by target identification by qRT-PCR is labor-intensive, requires amplification, and can suffer from sequence biases (7). Alternatively, microarray diagnostics exhibit low selectivity and limited dynamic range (8), and sequencing approaches require elaborate sample processing, expensive equipment, long wait times, and bioinformatic expertise, all of which limit their use. Electrochemical and single-molecule approaches are capable of ultrasensitive (<1 pM) (9) and amplification-free miR detection with a simple readout (10–12). However, developing a diagnostic that is ultrasensitive and highly selective is necessary to effectively discriminate low concentrations of similar-sequence nucleic acids. Furthermore, a diagnostic assay that does not require enzymatic amplification, preincubation, or washing is desirable for point-of-care use. To address these limitations, we report here a simple biosensor platform for miR detection that is capable of rapid digital signal accumulation with a wide dynamic range and highly selective single-base mismatch discrimination using DNA nanotechnology.

The progress of dynamic DNA nanotechnology has been tremendous, with clinical applications found in DNA hybridization imaging and diagnostics (13–16). By tuning the probe-target reaction entropy (ΔS) and enthalpy (ΔH), highly selective nucleic acid detection is achievable, with single-base discrimination (14, 17–19). Moreover, energetically tuned DNA hybridization probes can recognize single-base changes under large salinity, temperature, and concentration changes (14).

Whereas DNA probes can be designed to be highly discriminatory toward nucleic acid variants, photonic biosensors can achieve single-particle resolution by absorption amplification of bound nanoparticles (20, 21). Therefore, we combined the performance of selective DNA hybridization probes with digitally precise photonic crystal (PC) biosensors to directly detect target

Significance

Highly selective and sensitive detection of microRNA is a key challenge in the development of liquid-biopsy approaches. Technologies that can achieve high diagnostic performance without the requirement of complicated processing steps or expensive equipment are necessary for broad use. With these features in mind, we demonstrate a digital-readout microRNA diagnostic that fundamentally relies on microRNA-activated nanoparticle-photonic crystal hybrid coupling. The hybrid formation allows for clear detection of single-particle binding events due to enhanced nanoparticle absorption at the binding location. Whereas the applied photonics lend the assay concentration sensitivity, we additionally demonstrate broad placement single-base mismatch selectivity and complex media detection by applying free-energy tuned toehold probes.

Author contributions: T.D.C., N.L., and B.T.C. designed research; T.D.C. and N.L. performed research; L.D.S. contributed new reagents/analytic tools; T.D.C., N.L., L.D.S., Y.L., M.K., A.M.S., and B.T.C. analyzed data; and T.D.C. and N.L. wrote the paper.

The authors declare no conflict of interest.

This article is a PNAS Direct Submission.

[1]T.D.C. and N.L. contributed equally to this work.

[2]To whom correspondence may be addressed. Email: bcunning@illinois.edu.

This article contains supporting information online at www.pnas.org/lookup/suppl/doi:10.1073/pnas.1904770116/-/DCSupplemental.

First published September 9, 2019.

miRs with single mismatch discrimination capability and high concentration sensitivity.

Results

Photonic Resonator Absorption Microscopy for miR Diagnostics. We report a simple biosensor platform that is capable of rapid digital signal accumulation and highly selective miR mismatch discrimination. Furthermore, the assay is sensitive and dynamic enough to detect patient plasma/serum miR, which is normally in the femtomolar to low picomolar range (22). Following recent work associating miR-375 and -1290 levels in serum/plasma with prostate cancer metastasis, aggressiveness, and overall survival (23–26), we selected these 2 biomarkers as initial targets in our diagnostic platform. Moreover, miR-375 overexpression has been shown to induce docetaxel chemo-resistance, indicating that it may serve as a potential predictive biomarker in docetaxel-based chemotherapy in castration-resistance prostate cancer treatment (27). The PC used here is a subwavelength periodic grating structure which is highly sensitive to the presence plasmonic nanoparticle surface binding in its evanescent field when the PC resonance wavelength and the plasmonic nanoparticle resonance are matched (*SI Appendix*, Fig. S1) (28). The miR-specific DNA probe was stoichiometrically conjugated to a 100-nm-diameter gold nanoparticle (AuNP) (Fig. 1*A* and *SI Appendix*, Fig. S2), creating an miR plasmonic tag with a localized surface plasmon-resonance (SPR) wavelength of ∼625 nm, which coincides with the PC resonant wavelength. Activation of the DNA–AuNP tag by the miR initiated at a 7-base toehold site (Fig. 1*B*) and led to the strand displacement of a probe-protector strand (Fig. 1*C*) (29). The loss of the protector DNA exposed an additional probe sequence that stabilized binding to the surface 10-base PC capture DNA (Fig. 1*D*). Following target (miR) "activation," individual (i.e., digital) AuNP tags were bound (Fig. 1*E*). Single bound particles demonstrated localized enhanced light absorption, which produced a measurable shift in the PC resonant wavelength (Fig. 1*F*). All sequences used in this study are contained in *SI Appendix*, Table S1.

By matching the AuNP SPR to the PC-guided resonance (PCGR) wavelength, the synergistic coupling between the 2 resonators resulted in a drastically enhanced AuNP absorption cross-section (*SI Appendix*, Fig. S3) (30, 31). Specifically, the PCGR efficiently collected incident and particle-scattered light, thereby providing the AuNP with increased excitation through near-field coupling. Further, we applied AuNPs with a protruding tip morphology (Fig. 2*A*), which allowed for improved light harvesting across the particle surface (32). In contrast to gold nanorods, which demonstrate orientation-dependent enhancement upon PC binding (30), the AuNPs used herein demonstrate isotropic enhancement. The numerical simulation in Fig. 2*B* demonstrates the near-field intensity distribution of the PC–AuNP system with $\sim 10^4$ field enhancement at the AuNP sharp tip features and is shown to be sensitive to the incident angle and wavelength (*SI Appendix*, Fig. S4). The strong AuNP light absorption resulted in

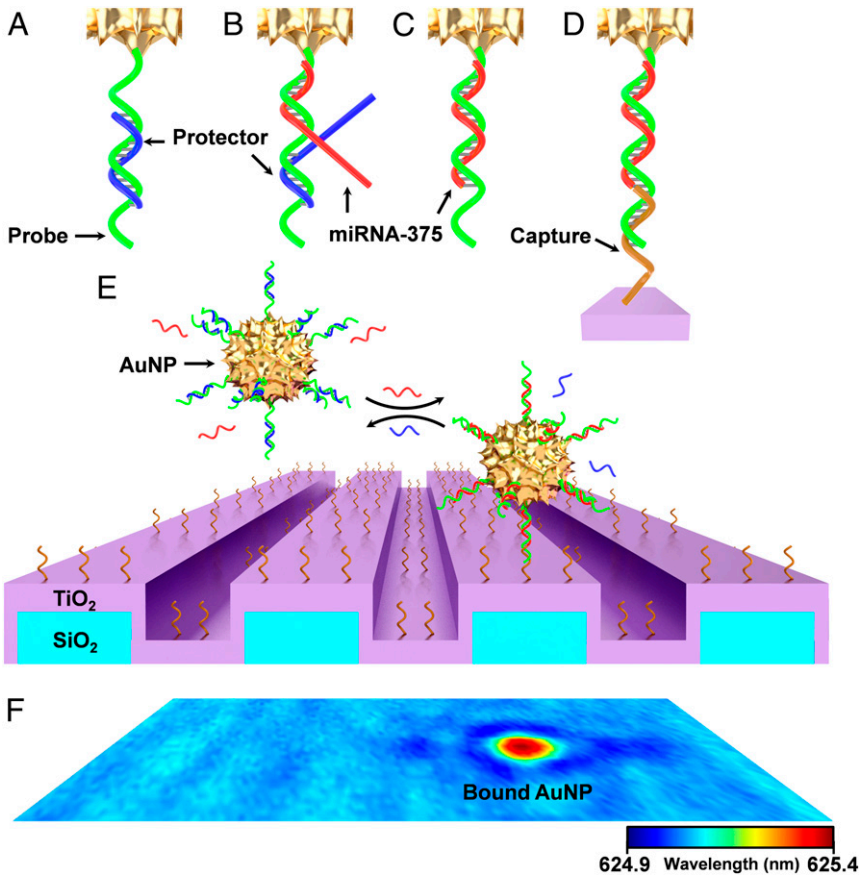

Fig. 1. Components of the toehold DNA–AuNP and miR detection by PC biosensors. DNA hybridization probes are conjugated to 100-nm diameter AuNPs. (*A*) The gold-conjugated DNA probe (green) is bound by a partially complementary protector (blue) preventing binding to the PC sensor (purple/blue structure). (*B*–*D*) miR (red) binds at the probe toehold (*B*), resulting in strand displacement of the protector and exposing additional probe sequence (C), which (*D*) stabilizes probe binding to the PC capture DNA on the biosensor surface (*D*). The free energy of the activation reaction can be tuned by the protector (blue) stoichiometry, thus enhancing mismatch selectivity. (*E* and *F*) Bound particles (*E*) can be measured by a shift in the PC resonance wavelength (*F*). All images are not to scale. The PRAM assay images the number of surface-captured particles over time (after miR addition).

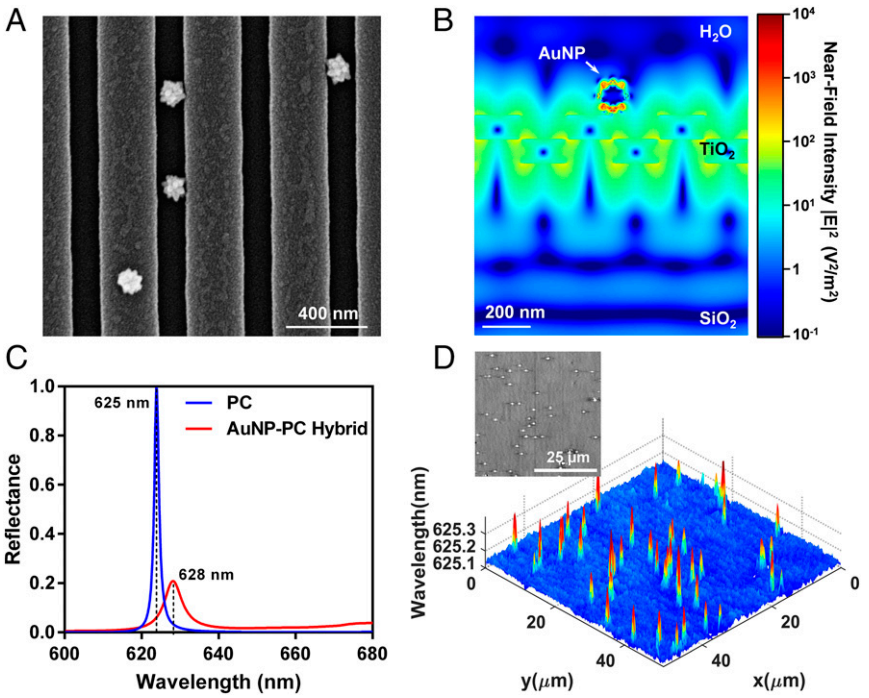

Fig. 2. AuNP–PC structure and coupling behavior. (*A*) SEM image of probe-conjugated AuNPs (100 nm) bound to the PC biosensor. (*B*) Finite-difference time-domain simulation of near-field intensity distribution of the AuNP–PC hybrid. (*C*) Simulated reflectance spectrum of the PC alone (blue) and the AuNP–PC hybrid (red). According to simulation, hybrid formation results in a reflectance peak wavelength shift ($\Delta\lambda$) to 628 nm from 625 nm and a reflectance peak intensity drop (ΔI). (*D*) The experimental 2D gray-scale PRAM image (*Upper Left*) is represented in the 3D contour plot (*Lower Right*), demonstrating the individual AuNP peak wavelength shifts.

an easily measurable, localized reduction in PC reflection intensity (ΔI) (Fig. 2*C*). Moreover, the formation of the AuNP–PC hybrid altered the resonance reflection wavelength ($\Delta\lambda$) due to hybrid coupling between the SPR and PCGR (Fig. 2*C*) (20, 30). The reflection peak wavelength shift ($\Delta\lambda$) was observable for each surface-attached AuNP (Fig. 2*D*), thereby allowing for "digital" AuNP optical quantification and enabling a form of microscopy we named Photonic Resonator Absorption Microscopy (PRAM; optical setup is in *SI Appendix*, Fig. S5).

DNA Probe Design and Energy Tuning. The DNA conjugated to the AuNP is a toehold probe specific for prostate cancer biomarker miR. Following recent guidelines in robust probe construction (14), we designed the reaction free energy (ΔG_{rxn}) between the DNA probe and the miR target to be approximately zero ($\Delta G_{rxn} \sim 0$). At $\Delta G_{rxn} \sim 0$, the average energetic penalty of a single mismatch is larger ($\Delta\Delta G$) than the free-energy gain of the perfect match, thereby limiting the off-target binding. We used the webtool NUPACK (33) to design a probe-protector duplex with limited, but still favorable, hybridization (reaction) free-energy gain to the target miR (*SI Appendix*, Table S2). As expected by Le Chatelier's principle, we added a stochiometric excess of the protector strand (strand-displacement product) to further tune the reaction toward $\Delta G_{rxn} \sim 0$ (34).

miR-375 Detection Using PRAM. The solution components of the assay are (*i*) DNA–AuNP, (*ii*) miR, (*iii*) excess protector (P_o), (*iv*) PC-DNA capture, and (*v*) buffer. We initially tested miR-375 on our platform. The assay was performed by mixing a constant amount of DNA–AuNP with a defined concentration of miR-375 in a PC-adhered polydimethylsiloxane well (~10 μL per well). Immediately following the introduction of mi-375, a 50 × 50-μm^2 PC surface area was scanned at a 30-min interval for up to 2 h (Fig. 3*A*). The PC-bound AuNPs were resolvable at single-particle digital resolution (Fig. 3*B*). To determine the particle count over time, we obtained the peak wavelength value (PWV) across all pixels in the field, followed by a series of image-processing steps, and a final watershed algorithm quantification step (*SI Appendix*, Fig. S6). We selected to process PWV images because the nanoparticles exhibited sharp features (*SI Appendix*, Fig. S6*B*), which is expected because the wavelength shift is the exclusive result of the formation of the AuNP–PC hybrid (20). In contrast, peak wavelength value (PIV) images represent the intensity of reflected light, which can be affected by the nonuniform illumination from the PC excitation profile, leading to elongated nanoparticle patterns along 1 dimension. Specifically, a nonuniform illumination will move the center of the Fourier plane toward higher frequencies collected by the objective, resulting in the observed side-lobe features in the PIV images (35). The PIV side-lobe features make accurate nanoparticle recognition and enumeration difficult. Following this, Fig. 3*C* shows the quantified PWV AuNP counts over time as a function of serially diluted miR concentration, with 100 aM and 10 pM representing the lowest (excluding no miR) and highest concentrations measured, respectively. We interpreted the increasing count time course to be the result of the coupled kinetic dependence of the toehold strand-displacement reaction and the surface capture of the activated DNA–AuNP on the miR-375 concentration. Unfortunately, we observed high nanoparticle background (>150) when no miR-375 was present. We hypothesized that the nonspecific background was likely due to direct hybridization between unprotected probe bases and the DNA capture (36). To test this, we added a 5-base DNA blocker (10 nM) to the DNA–AuNP/miR mixture, which was designed to bind the 10-base capture strand (36). With the addition of the DNA blocker, we observed <10 counts of nonspecific background in the no–miR-375 case, measured at 2 h. Furthermore, the addition of the DNA blocker did not compromise the ability to detect low concentrations of miR-375 (*SI Appendix*, Fig. S7).

Single-Mismatch miR-375 Discrimination. To test for selectivity, we investigated 5 different single-mismatch variants [single nucleotide variants (SNVs)] of miR-375, represented by MM_x (x = mismatch

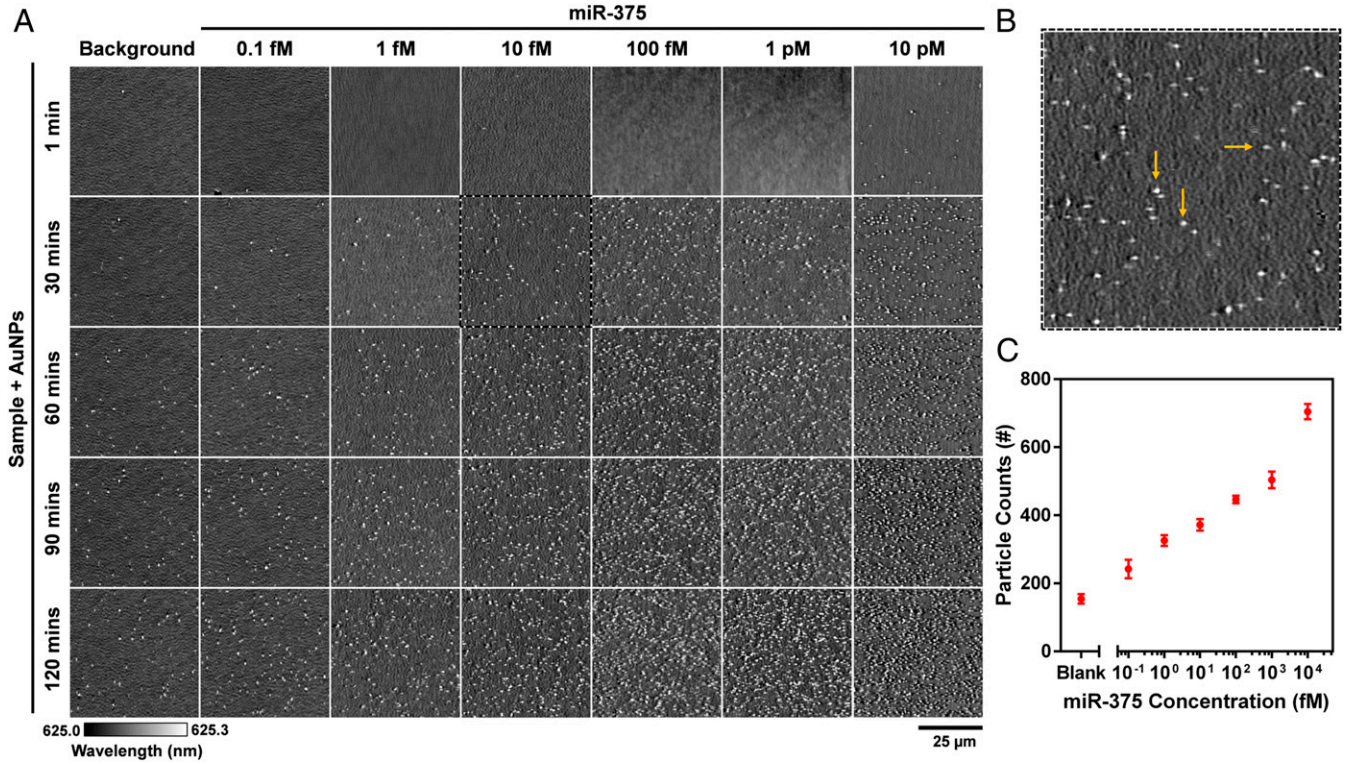

Fig. 3. Kinetic discrimination of miR-375 concentration using PRAM. (*A*) Peak wavelength gray-scale image panel demonstrates digital resolution of activated AuNPs as a function of miR-375 concentration (columns) over time (rows). Background (first column) scans represent the no–miR-375 control. (*B*) Expanded single tile from *A* (dashed tile) with added identifiers (yellow arrows) of representative single AuNPs. (*C*) Quantification of particle count as a function of miR-375 concentration at 2 h. Blank represents the no–miR-375 control. Each data point represents the average of 3 independent experiments. Error bars represent SEs.

position counted from 5′ end; *SI Appendix*, Table S1) in the PRAM assay. Fig. 4*A* demonstrates that all 5 SNVs resulted in a dramatic decrease in particle count over time, with a range of ∼83–94% signal reduction at 2 h (Fig. 4*B*). The complete time-course SNV image panel is shown in *SI Appendix*, Fig. S8. MM_1 (U > C) demonstrated the highest count, which we interpreted to be the result of the low terminal mismatch penalty. Therefore, irrespective of the first-base penalty, strand displacement was driven forward by the nucleation to the remaining 6 bases of downstream toehold. Additionally, we observed less than 60 AuNP counts at the 2-h scan for all SNVs tested, which was less than the background (no miR) count of ∼175 counts presented in Fig. 3*B*. This may hint that the SNVs nonspecifically bind to the PC capture, the AuNP surface, or conjugated probe. In either case, this would present a kinetic barrier to stable AuNP surface binding, thereby lowering the observed count.

Although an ∼83% reduction is acceptable, we investigated if we could further increase the binding discrimination between miR-375 (perfect match) and MM_1. To do so, we used a previously developed method of stoichiometric protector tuning to improve the reaction yield between the mismatch and perfect match (34). With a known mismatch $\Delta\Delta G$ (calculated by NUPACK), optimal perfect match versus mismatch discrimination occurs at a perfect match $\Delta G_{rxn} \sim -\frac{1}{2}\Delta\Delta G$. Following this, we calculated the optimal protector stoichiometry (*SI Appendix*, Table S3) for MM_1 discrimination. Fig. 4*C* demonstrates the improved PM discrimination from ∼5.6- to ∼6.7-fold above MM_1, using the protector stoichiometric tuning approach. The tuned protector stoichiometry was lower than the stoichiometry used in the $\Delta G_{rxn} \sim 0$ strategy (Fig. 4*B*), thereby making both the perfect and mismatch reactions more favorable, as seen by the count increase in both target cases (Fig. 4*C*). To this end, the tuned perfect-match case resulted in AuNP–PC-surface saturation in 2 h, thereby limiting the discrimination ratio improvement.

To test the binding stringency of DNA–AuNP for miR-375, we measured a serially decreasing concentration (100 aM, 1 fM, and 10 fM) of miR-375 in a relatively high concentration (1 pM) of mismatch (MM_5 was used here). Regardless of the relatively high mismatch background, we observed increasing AuNP counts as a function of increasing miR-375 frequency and assay time (*SI Appendix*, Fig. S9), with a maximum difference occurring at 2 h (Fig. 5*A*). The average total count across time for each was lower than the data in Fig. 3 by ∼50% (Fig. 5*B*). Again, this implies that the mismatch miR alters the perfect match (miR-375) kinetics by nonspecific binding. In addition to potential nonspecific binding of the capture oligonucleotide, the mismatch miR may transiently occupy the toehold site. However, as evidenced by the increase in counts as the miR concentration increased, spuriously bound miRs are expected to be driven off by mismatch destabilization and cognately bind miR-375. To further challenge the assay, we tested "spiked-in" miR-375 detection in a total RNA from healthy donor plasma. In brief, we added a defined concentration of synthetic miR-375 into a salt-buffered 100 pg/μL total RNA with stochiometric tuned DNA–AuNPs ($\Delta G_{rxn} \sim 0$ for miR-375) and scanned the PC biosensor at a 30-min interval for up to 2 h (*SI Appendix*, Fig. S10). An increasing number of AuNP counts over time (Fig. 5*C*) was observed for miR-375 additions of 1, 10, and 100 fM in the total RNA background (Fig. 5*D*). In the absence of miR-375, negligible counts (<5) were measured in the total RNA solution. Nevertheless, there was a drastic reduction in the particle count across all concentrations tested, which was likely due to greater nonspecific binding in the $\sim 10^5$ more dense total RNA background compared to the 1-pM

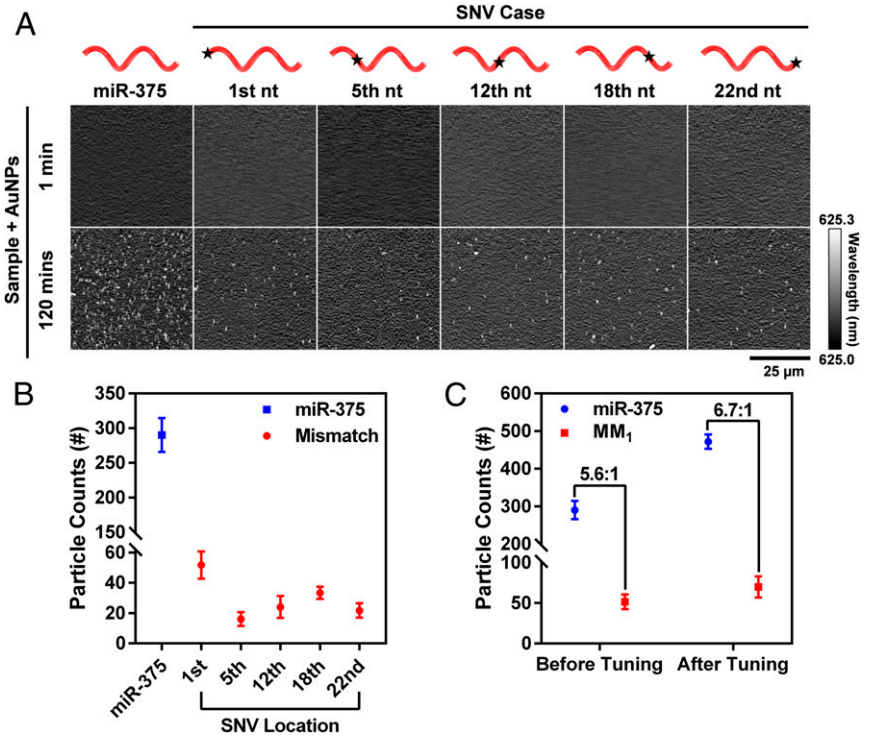

Fig. 4. Single-mismatch miR-375 discrimination. (*A*) Peak wavelength gray-scale image panel demonstrates particle count of miR-375 (first column) versus 5 different SNVs (columns) over time (rows). The mismatch placements in the sequence are representatively shown above (black stars). SNV mismatch location is given by the nucleotide (nt) position from the 5′ end. (*B*) AuNP count quantification of miR-375 and the SNV cases. (*C*) Considering the $\Delta\Delta G$ between the perfect match (miR-375) and MM_1, we calculated the necessary protector stoichiometry to optimize mismatch discrimination from ∼5.6- to ∼6.7-fold. Each data point in *B* and *C* represents the average of 3 independent experiments. Error bars represent SEs.

mismatch (MM_5) background demonstrated in Fig. 5*B*. To this end, the incorporation of a DNA-based signal amplifier (37) or magnetic particle DNA probes (11) into the overall PC assay design may aid in future detection without compromising short readout time or introducing unnecessary system complexity.

miR-1290 Detection Using PRAM. To explore the generality of the PRAM assay, we designed an additional probe for miR-1290, using the above strategy of stochiometric addition of an auxiliary protector probe to drive the free energy of reaction to zero ($\Delta G_{rxn} \sim 0$) (*SI Appendix*, Table S4). Motivated by the effectiveness of the miR-375

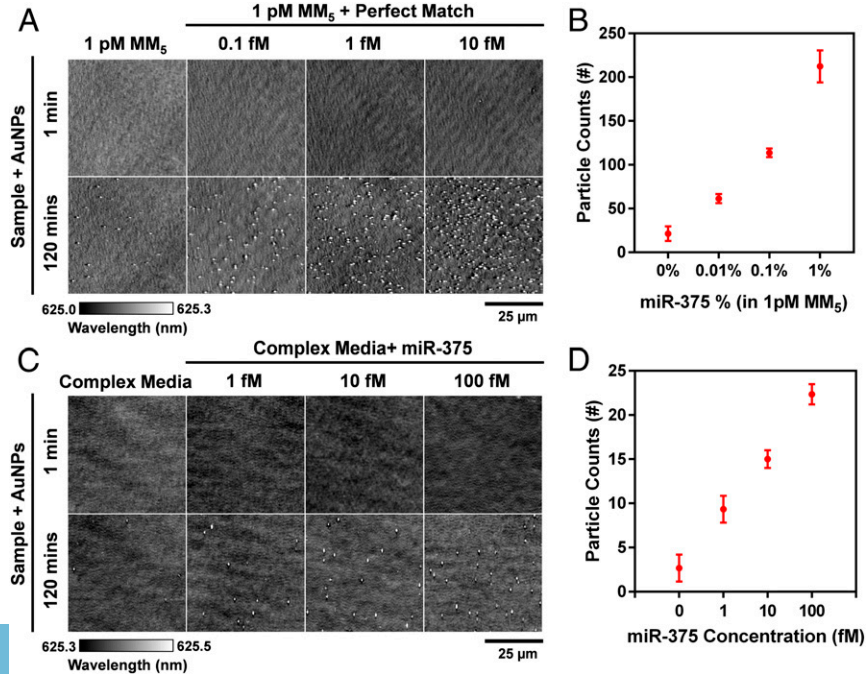

Fig. 5. miR-375 detection in a high-concentration mismatch background. (*A*) Variable concentration of miR-375 (columns) is added to a 1-pM mismatch (MM_5 was used for all tests) solution and scanned over time (rows). The first column represents mismatch alone (no miR-375). (*B*) Particle-count quantification is shown as a function of miR-375 concentration frequency ([miR-375]/[MM_5]). (*C*) Spiked concentrations of miR-375 within a total RNA background from healthy donor plasma are scanned over time. (*D*) Particle count is shown for 3 miR-375 concentrations and a no–miR-375 control. Each data point represents the average of 3 independent experiments. Error bars represent SEs.

DNA blocker in minimizing nonspecific binding, we applied a 5-base DNA blocker for all experiments involved in miR-1290 detection. Following the exact assay procedure as for miR-375 given above, we challenged our assay to detect miR-1290 at 100 aM, 10 fM, and 1 pM (including a no-target control). At the 2-h endpoint, we observed a concentration-dependent increase in particle count (*SI Appendix*, Fig. S11). In addition, we observed nearly zero background in the no-target control, likely due to the DNA blocker preventing nontarget activated particle binding. Lastly, we tested the probe selectivity by introducing a single mismatch at the 12th position (A > U) of miR-1290. With a single mismatch miR-1290 incubated at 1 pM, we observed an average of ~15 counts at the 2-h endpoint, which was significantly less than the >450 counts generated by the 1 pM miR-1290 perfect match at same time point (*SI Appendix*, Fig. S11).

Conclusions

We have demonstrated that by integrating principled DNA nanotechnology with PC biosensors, highly selective and sensitive diagnostics is achievable, where each miR target molecule translates into a digitally observable nanoparticle attachment to the PC, via 2 highly specific biomolecular recognition events. The assay was conducted at room temperature, without any target amplification or wash steps. Single mismatches can be located across the candidate miR when using a DNA probe/protector system that is free-energy tuned. The digital-resolution capability of the PRAM biosensor microscopy allows for direct, dynamic, rapid, and clinically relevant subfemtomolar signal accumulation and miR detection. Given the simplicity of assay and the commercial availability (with low cost) of the reagents involved, we expect that the PRAM method can be applied to detect DNA, proteins, and small molecules as well. As a step toward this, we demonstrated ultrasensitive miR detection in a complex total RNA background. Lastly, through the PC-mediated enhanced absorption, we achieved digital detection of AuNPs, which we expect can be implemented in a low-cost and portable point-of-care device.

Materials and Methods

The materials and methods used in this study are described in detail in *SI Appendix, SI Materials and Methods*. We included information on PC fabrication and capture DNA functionalization, nucleic acid sequence, AuNP probe preparation, biosensor functionalization, image analysis, and RNA plasma extraction.

ACKNOWLEDGMENTS. This work was supported by the Institute for Genomic Biology (IGB) and NIH Grants 5R33CA177446-02 and 5R01GM086382-03. T.D.C. is supported by an IGB Fellowship within the Omics Nanotechnology for Cancer Precision Medicine theme. Support for time and effort in part was provided by NIH–National Cancer Institute Grants R01 CA21209 and R01CA227699 (to M.K.).

1. S. K. Vashist, P. B. Luppa, L. Y. Yeo, A. Ozcan, J. H. T. Luong, Emerging technologies for next-generation point-of-care testing. *Trends Biotechnol.* **33**, 692–705 (2015).
2. J. Donaldson, B. H. Park, Circulating tumor DNA: Measurement and clinical utility. *Annu. Rev. Med.* **69**, 223–234 (2018).
3. P. S. Mitchell *et al.*, Circulating microRNAs as stable blood-based markers for cancer detection. *Proc. Natl. Acad. Sci. U.S.A.* **105**, 10513–10518 (2008).
4. C. Bettegowda *et al.*, Detection of circulating tumor DNA in early- and late-stage human malignancies. *Sci. Transl. Med.* **6**, 224ra24 (2014).
5. C. Ortholan *et al.*, MicroRNAs and lung cancer: New oncogenes and tumor suppressors, new prognostic factors and potential therapeutic targets. *Curr. Med. Chem.* **16**, 1047–1061 (2009).
6. R. Rosell, J. Wei, M. Taron, Circulating microRNA signatures of tumor-derived exosomes for early diagnosis of non-small-cell lung cancer. *Clin. Lung Cancer* **10**, 8–9 (2009).
7. V. El-Khoury, S. Pierson, T. Kaoma, F. Bernardin, G. Berchem, Assessing cellular and circulating miRNA recovery: The impact of the RNA isolation method and the quantity of input material. *Sci. Rep.* **6**, 19529 (2016).
8. E. A. Hunt, D. Broyles, T. Head, S. K. Deo, MicroRNA detection: Current technology and research strategies. *Annu. Rev. Anal. Chem. (Palo Alto, Calif.)* **8**, 217–237 (2015).
9. Y. Wu, R. D. Tilley, J. J. Gooding, Challenges and solutions in developing ultrasensitive biosensors. *J. Am. Chem. Soc.* **141**, 1162–1170 (2019).
10. M. Labib, E. H. Sargent, S. O. Kelley, Electrochemical methods for the analysis of clinically relevant biomolecules. *Chem. Rev.* **116**, 9001–9090 (2016).
11. R. Tavallaie *et al.*, Nucleic acid hybridization on an electrically reconfigurable network of gold-coated magnetic nanoparticles enables microRNA detection in blood. *Nat. Nanotechnol.* **13**, 1066–1071 (2018).
12. A. Johnson-Buck *et al.*, Kinetic fingerprinting to identify and count single nucleic acids. *Nat. Biotechnol.* **33**, 730–732 (2015).
13. E. Lubeck, A. F. Coskun, T. Zhiyentayev, M. Ahmad, L. Cai, Single-cell in situ RNA profiling by sequential hybridization. *Nat. Methods* **11**, 360–361 (2014).
14. D. Y. Zhang, S. X. Chen, P. Yin, Optimizing the specificity of nucleic acid hybridization. *Nat. Chem.* **4**, 208–214 (2012).
15. S. X. Chen, D. Y. Zhang, G. Seelig, Conditionally fluorescent molecular probes for detecting single base changes in double-stranded DNA. *Nat. Chem.* **5**, 782–789 (2013).
16. R. M. Dirks, N. A. Pierce, Triggered amplification by hybridization chain reaction. *Proc. Natl. Acad. Sci. U.S.A.* **101**, 15275–15278 (2004).
17. J. Zheng *et al.*, Rationally designed molecular beacons for bioanalytical and biomedical applications. *Chem. Soc. Rev.* **44**, 3036–3055 (2015).
18. G. Bonnet, S. Tyagi, A. Libchaber, F. R. Kramer, Thermodynamic basis of the enhanced specificity of structured DNA probes. *Proc. Natl. Acad. Sci. U.S.A.* **96**, 6171–6176 (1999).
19. D. A. Khodakov, A. S. Khodakova, D. M. Huang, A. Linacre, A. V. Ellis, Protected DNA strand displacement for enhanced single nucleotide discrimination in double-stranded DNA. *Sci. Rep.* **5**, 8721 (2015).
20. Y. Zhuo *et al.*, Single nanoparticle detection using photonic crystal enhanced microscopy. *Analyst (Lond.)* **139**, 1007–1015 (2014).
21. D. Sevenler, G. G. Daaboul, F. Ekiz Kanik, N. L. Ünlü, M. S. Ünlü, Digital microarrays: Single-molecule readout with interferometric detection of plasmonic nanorod labels. *ACS Nano* **12**, 5880–5887 (2018).
22. Z. Williams *et al.*, Comprehensive profiling of circulating microRNA via small RNA sequencing of cDNA libraries reveals biomarker potential and limitations. *Proc. Natl. Acad. Sci. U.S.A.* **110**, 4255–4260 (2013).
23. X. Huang *et al.*, Exosomal miR-1290 and miR-375 as prognostic markers in castration-resistant prostate cancer. *Eur. Urol.* **67**, 33–41 (2015).
24. D. Kachakova *et al.*, Combinations of serum prostate-specific antigen and plasma expression levels of let-7c, miR-30c, miR-141, and miR-375 as potential better diagnostic biomarkers for prostate cancer. *DNA Cell Biol.* **34**, 189–200 (2015).
25. H. C. Nguyen *et al.*, Expression differences of circulating microRNAs in metastatic castration resistant prostate cancer and low-risk, localized prostate cancer. *Prostate* **73**, 346–354 (2013).
26. S. Wach *et al.*, The combined serum levels of miR-375 and urokinase plasminogen activator receptor are suggested as diagnostic and prognostic biomarkers in prostate cancer. *Int. J. Cancer* **137**, 1406–1416 (2015).
27. Y. Wang *et al.*, miR-375 induces docetaxel resistance in prostate cancer by targeting SEC23A and YAP1. *Mol. Cancer* **15**, 70 (2016).
28. H. Inan *et al.*, Photonic crystals: Emerging biosensors and their promise for point-of-care applications. *Chem. Soc. Rev.* **46**, 366–388 (2017).
29. D. Y. Zhang, G. Seelig, Dynamic DNA nanotechnology using strand-displacement reactions. *Nat. Chem.* **3**, 103–113 (2011).
30. J. N. Liu, Q. Huang, K. K. Liu, S. Singamaneni, B. T. Cunningham, Nanoantenna-microcavity hybrids with highly cooperative plasmonic-photonic coupling. *Nano Lett.* **17**, 7569–7577 (2017).
31. Q. Huang, B. T. Cunningham, Microcavity-mediated spectrally tunable amplification of absorption in plasmonic nanoantennas. *Nano Lett.* **19**, 5297–5303 (2019).
32. F. Hao, C. L. Nehl, J. H. Hafner, P. Nordlander, Plasmon resonances of a gold nanostar. *Nano Lett.* **7**, 729–732 (2007).
33. R. M. Dirks, J. S. Bois, J. M. Schaeffer, E. Winfree, N. A. Pierce, Thermodynamic analysis of interacting nucleic acid strands. *SIAM Rev.* **49**, 65–88 (2007).
34. L. R. Wu *et al.*, Continuously tunable nucleic acid hybridization probes. *Nat. Methods* **12**, 1191–1196 (2015).
35. F. Wei, Z. Liu, Plasmonic structured illumination microscopy. *Nano Lett.* **10**, 2531–2536 (2010).
36. A. Johnson-Buck, J. Li, M. Tewari, N. G. Walter, A guide to nucleic acid detection by single-molecule kinetic fingerprinting. *Methods* **153**, 3–12 (2019).
37. S. X. Chen, G. Seelig, An engineered kinetic amplification mechanism for single nucleotide variant discrimination by DNA hybridization probes. *J. Am. Chem. Soc.* **138**, 5076–5086 (2016).